

1-18-2018

## Lithography-Free, Omnidirectional, CMOS-Compatible AlCu Alloys for Thin-Film Superabsorbers

Mariama Rebello de Sousa Dias  
*University of Richmond*, [mdias@richmond.edu](mailto:mdias@richmond.edu)

Chen Gong

Zachary A. Benson

Marina S. Leite

Follow this and additional works at: <https://scholarship.richmond.edu/physics-faculty-publications>

 Part of the [Physics Commons](#)

---

### Recommended Citation

Dias, Mariama Rebello Sousa, Chen Gong, Zackery A. Benson, and Marina S. Leite. "Lithography-Free, Omnidirectional, CMOS-Compatible AlCu Alloys for Thin-Film Superabsorbers." *Advanced Optical Materials* 6, no. 2 (January 18, 2018): 1700830. <https://doi.org/10.1002/adom.201700830>.

This Article is brought to you for free and open access by the Physics at UR Scholarship Repository. It has been accepted for inclusion in Physics Faculty Publications by an authorized administrator of UR Scholarship Repository. For more information, please contact [scholarshiprepository@richmond.edu](mailto:scholarshiprepository@richmond.edu).

# Lithography-Free, Omnidirectional, CMOS-Compatible AlCu Alloys for Thin-Film Superabsorbers

Mariama Rebello Sousa Dias, Chen Gong, Zackery A. Benson, and Marina S. Leite\*


Superabsorbers based on metasurfaces have recently enabled the control of light at the nanoscale in unprecedented ways. Nevertheless, the sub-wavelength features needed to modify the absorption band usually require complex fabrication methods, such as electron-beam lithography. To overcome the scalability limitations associated with the fabrication of metallic nanostructures, engineering the optical response of superabsorbers by metal alloying is proposed, instead of tuning the geometry/size of the nanoscale building blocks. The superior performance of thin film AlCu alloys as the metallic component of planar bilayer superabsorbers is numerically demonstrated. This alloy outperforms its pure constituents as well as other metals, such as Ag, Au, and Cr. As a model system, a Si/AlCu structure is analyzed that presents >99% absorption at selected wavelength ranging from the visible to the near-infrared regions of the spectrum, depending on the subwavelength thickness of the semiconductor. The multi-wavelength near-unity absorption behavior of Si/AlCu persists even for oblique angle of incidence, up to 70°. Additionally, the findings are validated by fabricating and testing a-Si/AlCu superabsorbers, where good agreement is found between the numerically and experimentally determined optical response. The system investigated here is relevant for integration in complementary metal-oxide-semiconductor (CMOS) technologies.

Building blocks that ‘perfectly’ absorb electromagnetic radiation from ultraviolet (UV) to radio frequency have direct applications in thermal emission and detection,<sup>[1,2]</sup> thermoelectronics and thermophotovoltaics,<sup>[3–5]</sup> sensors,<sup>[6]</sup> and radar and stealth technology.<sup>[7,8]</sup> Superabsorbers (also termed perfect absorbers) are artificially constructed materials (or metamaterials) that present a resonance that corresponds to near unity absorbance over a

Dr. M. R. S. Dias, C. Gong, Z. A. Benson, Prof. M. S. Leite  
Institute for Research in Electronics and Applied Physics  
University of Maryland  
College Park, MD 20742, USA  
E-mail: mleite@umd.edu

C. Gong, Prof. M. S. Leite  
Department of Materials Science and Engineering  
University of Maryland  
College Park, MD 20742, USA

Z. A. Benson  
Department of Physics  
University of Maryland  
College Park, MD 20742, USA

 The ORCID identification number(s) for the author(s) of this article can be found under <https://doi.org/10.1002/adom.201700830>.

DOI: 10.1002/adom.201700830

single, multiple, or broadband frequency of the electromagnetic spectrum. The ultrahigh light absorption is obtained due to an impedance match between the material and the medium.<sup>[9]</sup> Here, the electric and magnetic resonances are designed so that the bulk effective impedance is equal to the one of the free space (air or vacuum). As a result, most of the incident light is absorbed and the reflection is negligible. Salisbury<sup>[10]</sup> and Dallenbach<sup>[11]</sup> first idealized classical absorbers to operate in the microwave range of the electromagnetic spectrum. The former included a resistive layer located at a quarter wavelength from a metallic substrate while the latter consisted of a dielectric layer on top of a metallic substrate.

In the past two decades, advances in nanofabrication have given rise to nanostructures with controlled geometry, recently inspiring the design of metamaterials and metasurfaces for superabsorbers.<sup>[12]</sup> With the flexibility of tuning nanostructures' geometry and periodicity, such absorbers have been demonstrated in the visible,<sup>[13,14]</sup> near-infrared (NIR),<sup>[15]</sup> mid-infrared (MIR),<sup>[16]</sup> and far-infrared (FIR)<sup>[17,18]</sup> frequency ranges, proving to be a powerful approach for producing optical responses that are not feasible by any conventional material. However, the cost of the current fabrication methods limits their commercial applications. For instance, metasurfaces consisting of arrays of nanostructures on a dielectric surface are difficult to manufacture through physical deposition approaches in large scale even by using state-of-the-art bottom-up nanolithography methods.

To overcome the scalability constraints of the fabrication methods currently implemented for metasurfaces, the use of thin films in superabsorbers has been explored for a broad range of the spectrum, extending from visible to the FIR.<sup>[19–28]</sup> The Dallenbach configuration provides significant benefits regarding the fabrication of ultrathin, planar, omnidirectional, and polarization independent structures with very high absorption. Recently, it was reported that more than 98% of the normally incident light could be absorbed in an ultrathin layer of Ge on top of Ag at a wavelength ( $\lambda$ ) of 625 nm, decreasing to 80% for incident angles up to 66° for both polarizations.<sup>[21]</sup> In addition, highly doped Si has been used as a metallic-like substrate under a thin Ge layer to absorb light in the MIR, where the doping concentration in Si was the knob to engineer its

dielectric function.<sup>[26]</sup> Further, GaAs on Au has been experimentally reported to absorb 96% of incident light at  $\lambda = 38 \mu\text{m}$ .<sup>[27]</sup>

To control the range of operation of metallic thin films and nanostructures for nanophotonics, alternative materials and geometries have been recently considered, such as metal alloys, transparent conducting oxides, transition metal nitrides, yttrium hydride, semiconductors, among others.<sup>[29–34]</sup> Specifically, the alloying of metals has allowed materials with optical responses unachievable by the individual metal components.<sup>[29]</sup> Imminent material options for on-chip nanophotonics rely on metals like Al and Cu due to their fully complementary metal–oxide–semiconductor (CMOS) compatibility and low-cost/earth abundance. These metals have well-defined permittivity with absorption at  $\lambda \approx 460$  and  $\approx 600$  nm, respectively. Therefore, mixing them could provide thin films with adjustable permittivity that complement the semiconductor layer for near-unity absorption in the thin film configuration.

Here, we demonstrate by analytic calculations and numerical simulations that near-unity absorption (>99%) is achieved in a bilayer planar configuration superabsorber composed of an alloyed metallic layer (with nominal composition of  $\text{Al}_{0.5}\text{Cu}_{0.5}$  or AlCu) and a semiconductor (Si, Ge, and GaAs). Using the transfer matrix method (TMM), we perform a quantitative and comparative analysis of the optical response of different metals, including Ag, Au, Cr, Al, Cu, and AlCu. We find that AlCu substantially outperforms those pure metals commonly used in photonics. The Si/AlCu system supports Brewster modes, where the high absorption resonance peak can be finely tuned from the visible to the NIR by simply varying the thickness of the semiconductor layer. Furthermore, we find that the planar structure of Si/AlCu is a dual-band superabsorber with the first and second modes in the NIR and the visible regions of the electromagnetic spectrum, respectively. As desired, the high absorption is independent of the polarization and spans a large oblique angle of the incident light. Additionally, by increasing the value of the index of refraction of the surrounding medium, the absorption maxima blue shifts while changing between optical modes. Finally, as a proof of concept, we fabricate a-Si/AlCu thin film superabsorbers and demonstrate that a single and dual-band near-unity absorption is obtained by adjusting the semiconductor thickness, in agreement with our simulations. Our results reveal the potential of thin film metal alloys in future nanophotonic applications, spanning from integrated optical circuits to sensing devices and thermo-photovoltaics.

A schematic illustration of the thin film superabsorbers investigated here is presented in the top row of **Figure 1**. The thin film thicknesses considered are  $d$  (variable) and  $h = 100$  nm for the Si top and the metallic bottom layers, respectively. Here, we choose Si as the semiconductor because of its CMOS compatibility. Also, the band gap energy of Si (at 1117 nm) lies in the NIR, enabling us to access the optical response of the absorber stack for energies lower than the semiconductor's band gap, where light is absorbed by the metal alloy, see absorptance maps in SI file (a process that is assisted by the refractive index contrast between Si and AlCu). We first compare the absorption profile of superabsorbers with adjustable Si thickness and using Ag, Au, Cr, Al, Cu, as well as AlCu. The permittivity of all metals is obtained experimentally by ellipsometry measurements (see the

Experimental Section for details) from thin film samples fabricated by sputtering (see Figures S1 and S2 and Table S1 in the Supporting Information for their optical properties and for the chemical composition analysis of the AlCu film, respectively). To minimize the contribution of metal oxidation due to air exposure, we perform the ellipsometry measurements immediately after the deposition of the thin films.

The absorber with the alloyed metallic layer outperforms all stacks containing pure metals with a remarkably higher absorption peak for a broad range of Si thicknesses, as displayed in Figure 1a–f (see Figure S3 in the Supporting Information for comparison between experimentally obtained and Palik's data). The absorption profile within the semiconductor/metal alloy stack is presented in Figure S4 in the Supporting Information, and shows strong light absorption in the AlCu layer, beyond the bandgap of Si, as expected. For the analysis of the first absorption resonant mode ( $m_1$ ), we consider the normal incidence absorption spectra as a function of  $d = 5$  to 75 nm (color-coded). In all cases,  $m_1$  redshifts as the film thickness  $d$  increases. Au has an absorption maximum of 94.85% for  $d = 10$  nm. The overall absorption of the noble metals lowers in the NIR range of the spectrum for thicker Si films (>40 nm). For Cr, the absorption peak of the superabsorber slightly increases in the NIR, reaching its maximum value (94.56%) at  $d = 75$  nm. Despite the fact that Si does not absorb beyond its band gap, its  $n$  value allows a resonance due to the non-trivial phase shift at the interface between Si and Cr, enhancing the overall absorption of the stack.<sup>[35]</sup> Pure Al and pure Cu present an absorption maximum of 97.07% and 98.50% in the visible range of the spectrum for  $d = 10$  and 15 nm, respectively, see Figure 1d,e. The superabsorber containing AlCu clearly holds the maximum absorption over a wide range of the electromagnetic spectrum. From  $d = 5$  to 75 nm, >98.16% of the light is absorbed, spanning visible to NIR wavelengths—as shown in Figure 1f. We attribute the unique optical response of the AlCu alloy in the NIR to a change in the band structure of the material.<sup>[36]</sup> In addition, it is likely that the small grains composing the film and their boundaries lead to increased absorption.<sup>[37,38]</sup> Thus, as a consequence, the permittivity's imaginary part presents a higher value than the pure metals (see Figure S2 in the Supporting Information).

Figure 1g–l presents the normal incidence absorption maps as a function of  $d$ , where four distinct modes ( $m_i$ ,  $i = 1$  to 4) are identified. As expected, for Au and Ag all modes with high absorption values are restricted to the visible range of the electromagnetic spectrum while decaying drastically over the NIR. Cr extends its high absorption response of  $m_1$  and  $m_2$  from the visible to the NIR (see Figure 1i). Al and Cu present a comparable behavior to noble metals in the visible while decaying modestly in the NIR (see Figure S5 in the Supporting Information for a quantitative comparison between the absorption maps of bare Si and the Si/metal stacks). Note that AlCu and Cr have similar characteristics: both extend their high absorption responses of  $m_1$  and  $m_2$  from the visible to the NIR (Figure 1l,i). Nevertheless, AlCu retains near-unity absorption (>99%) from  $\lambda = 409$  nm ( $d = 5.5$  nm) to  $\lambda = 1016$  nm ( $d = 47.6$  nm). Moreover, for  $d$  between 60 and 75 nm both modes,  $m_1$  and  $m_2$ , have its absorption >98.60%, making this structure a dual-band superabsorber with one peak in the visible and another in the NIR. Similarly, for Ge and GaAs,

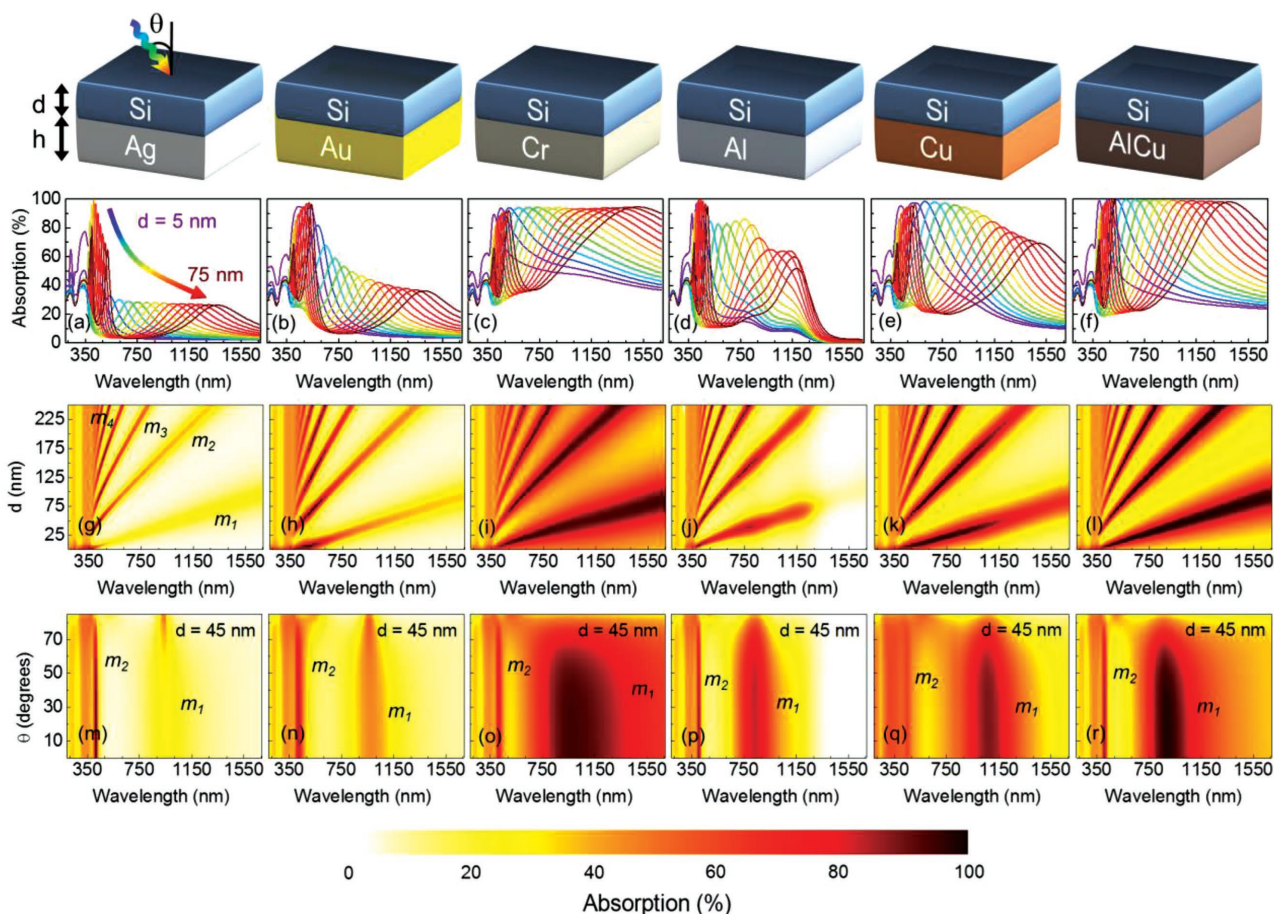


**Figure 1.** Subwavelength superabsorbers. Top row: schematic of the bilayer structure, where  $h = 100$  nm and  $d$  are the thicknesses of the metallic thin film (Ag, Au, Cr, Al, Cu, AlCu) and the Si layer, respectively.  $\theta$  is the angle of the incident light from the air. a–f) Calculated normal incidence absorption spectra as a function of  $d$  (color-coded). g–l) Calculated normal incidence absorption maps as a function of  $d$  showing optical modes ( $m_1$ ,  $m_2$ ,  $m_3$ ,  $m_4$ ). m–r) Calculated absorption maps as a function of  $\theta$  (here,  $d = 45$  nm).

near-unity absorption can also be obtained (see Figures S6–S10 in the Supporting Information). Commonly, a dual-band absorber is achieved by designing arrays of nanostructures.<sup>[39]</sup> The origin of the optical response of AlCu lies on both real ( $\epsilon_1$ ) and imaginary ( $\epsilon_2$ ) parts of the permittivity. The low magnitude of  $|\epsilon_1|$  over the entire spectrum is responsible for the strength of dynamical screening effects which, in combination with the large value of  $\epsilon_2$  (especially in the NIR), leads to a high absorption of AlCu.

One advantage of the planar configuration for superabsorbers is the wide oblique angular tolerance of its resonant peak.<sup>[12]</sup> Figure 1m–r displays the absorption maps as a function of the incident angle ( $\theta$ ) of an unpolarized light for  $d = 45$  nm. Ag and Au have an inferior response for the mode  $m_1$ , absorbing  $< 45\%$  of light in the NIR. However, for the mode  $m_2$ ,  $\approx 98\%$  and  $\approx 84\%$  is absorbed in the visible for Ag and Au, respectively. The angle dependent maps for Cr, Al, Cu, and AlCu show that the characteristic peaks  $m_1$  and  $m_2$  remain high for a large  $\theta$  ( $\geq 70^\circ$ ). The superior performance of the system containing the AlCu alloy strongly indicates its potential application in CMOS-compatible superabsorbers.

We quantitatively compare the absorption maps of Si/metal stacks with an arbitrary index of refraction ( $\tilde{n} = n + ik$ ) for the

metal; see **Figure 2**, where the selected wavelengths refer to the maximum absorption for the Si/AlCu stack with different semiconductor thickness shown in Figure 1a–f. We find that the stack with the AlCu alloy outperforms the ones formed by pure metals whenever the thickness of the semiconductor is  $\geq 15$  nm. The symbols in Figure 2 correspond to the refractive indices of Ag, Au, Cr, Al, Cu, and AlCu. In our calculations we consider an optimal thickness of  $h = 100$  nm for the metallic layer in order to eliminate the transmission signal of the system (see Figures S11 and S12 in the Supporting Information for details); thus, the performance of each metal can be independently evaluated. For all cases, AlCu offers the best alternative from all metals investigated (see Figure S13 in the Supporting Information for the performance of potentially CMOS-compatible metals). Figure 2a presents the results for a Si film thickness  $d = 5$  nm at wavelength  $\lambda = 400$  nm. Here, AlCu is the only material that fulfills the condition of near-unity absorption, where the maximum absorption is 98.99%. Figure 2b corresponds to  $d = 15$  nm at  $\lambda = 536$  nm with an absorption maximum of 99.74%. Likewise, for  $d = 45$  nm at  $\lambda = 970$  nm, AlCu presents maximum absorption of 99.13% (Figure 2c). Finally, for  $d = 75$  nm at  $\lambda = 1404$  nm, AlCu (98.16%), and Cr (92.92%)

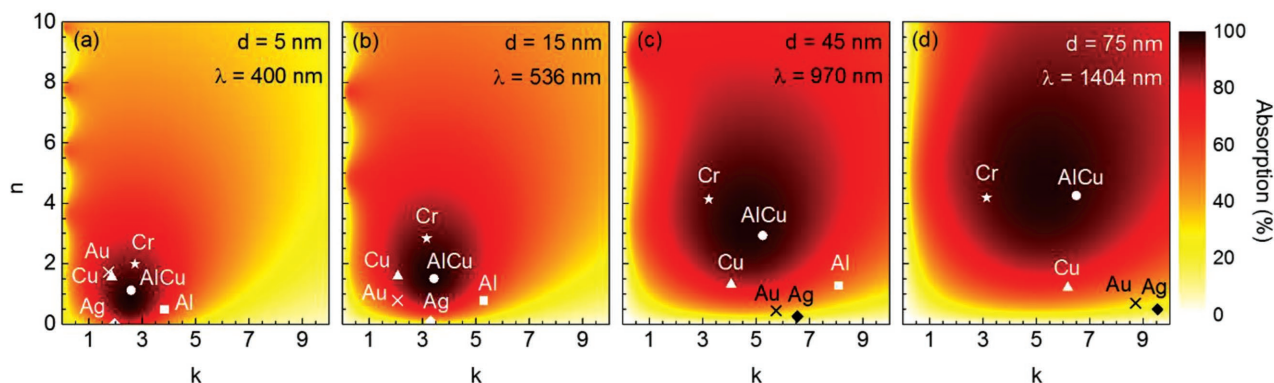


**Figure 2.** Calculated absorption maps of thin film absorbers (Si/metal layer) for materials with different refractive index ( $\tilde{n} = n + ik$ ). The performance of Ag, Au, Cr, Al, Cu, and AlCu are represented by a given symbol. The top Si layer has a variable thickness  $d$  of a) 5, b) 15, c) 45, and d) 75 nm. The bottom layer is fixed at 100 nm. The selected wavelengths refer to the maximum absorption of the Si/AlCu for each semiconductor thickness.

present comparable performance with high values for the absorption, as shown in Figure 2d.

To assess the possible effects of angle and light polarization on the optical response of the Si/AlCu system, we deconvolute these parameters by calculating the absorption profile for three different Si thicknesses. The planar configuration containing AlCu exhibits near-unity absorption that is insensitive to the incident angle and polarization, a desired feature for emitters and sensors. **Figure 3** displays the absorption maps as a function of  $\theta$  and  $\lambda$  for  $d = 15$  (Figure 3a–c), 45 (Figure 3d–f), and 75 nm (Figure 3g–i). In all cases, the absorption peak corresponding to  $m_1$  remains high over a large incident angle range. At  $\approx 50^\circ$ , 95% of the unpolarized light continues to be absorbed, decreasing slightly to 80% at  $\approx 70^\circ$  (Figure 3a,d,g). For oblique incidence, the  $s$ - and  $p$ -polarized light exhibit different responses. For  $s$ -polarized light, the mode

$m_1$  presents  $>95\%$  absorption for  $\theta$  up to  $\approx 60^\circ$  (see Figure 3b,e,h, respectively). For  $p$ -polarized light, the features are considerably different for the three Si thicknesses considered. Figure 3c corresponds to  $d = 15$  nm, where the absorption of  $m_1$  persists high for  $\theta$  up to  $41^\circ$  ( $>95\%$ ) while for  $\theta > 81^\circ$   $m_2$  ( $\lambda \approx 345$  nm) exceeds this value ( $>98\%$ ). Figure 3f shows the characteristics of  $d = 45$  nm, where more than 95% of the incident light is absorbed over  $35^\circ$ , while for  $\theta \geq 40^\circ$  the absorption maximum blue shifts to  $m_2$  ( $\lambda \approx 193$  nm). Finally, Figure 3i displays the high absorption for  $d = 75$  nm corresponding to  $m_1$  ( $\lambda \approx 1310$  nm) over  $24^\circ$ , to  $m_2$  up to  $50^\circ$  ( $\lambda \approx 504$  nm), and to  $m_3$  for  $64^\circ < \theta < 84^\circ$  ( $\lambda \approx 395$  nm). These results illustrate the effective high performance of the semiconductor/metal alloy model system investigated here, including in situations where incident light is oblique, applicable for thermophotovoltaics and bolometers.

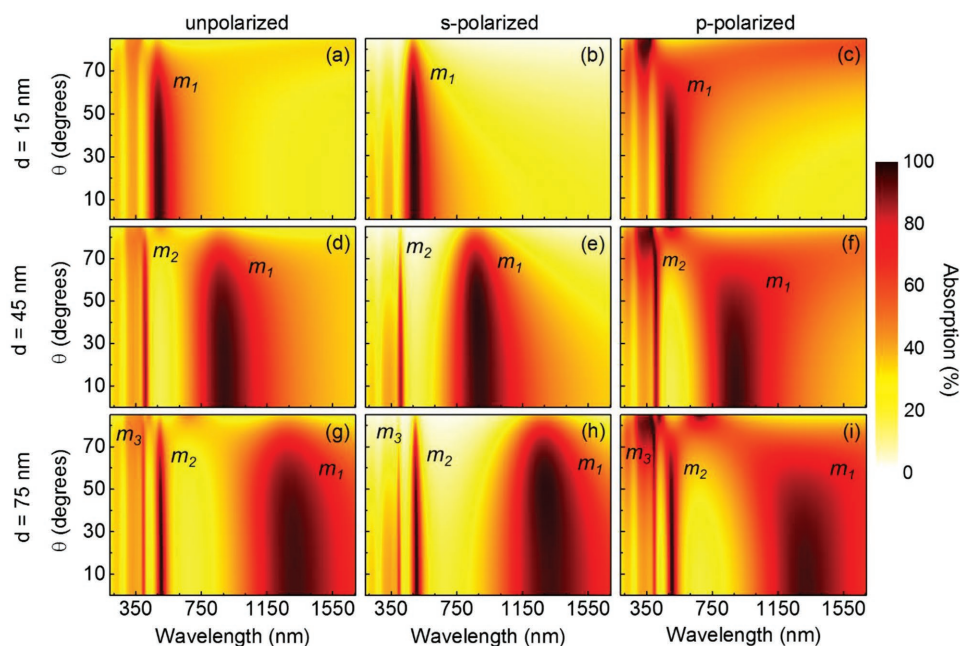


**Figure 3.** Near-unity absorption sensitiveness to polarization and incident angle. Polarization dependent absorption maps calculated as a function of incident angle  $\theta$  and wavelength for 100 nm AlCu metallic film coated with a–c) 15, d–f) 45, and g,h) 75 nm Si films.

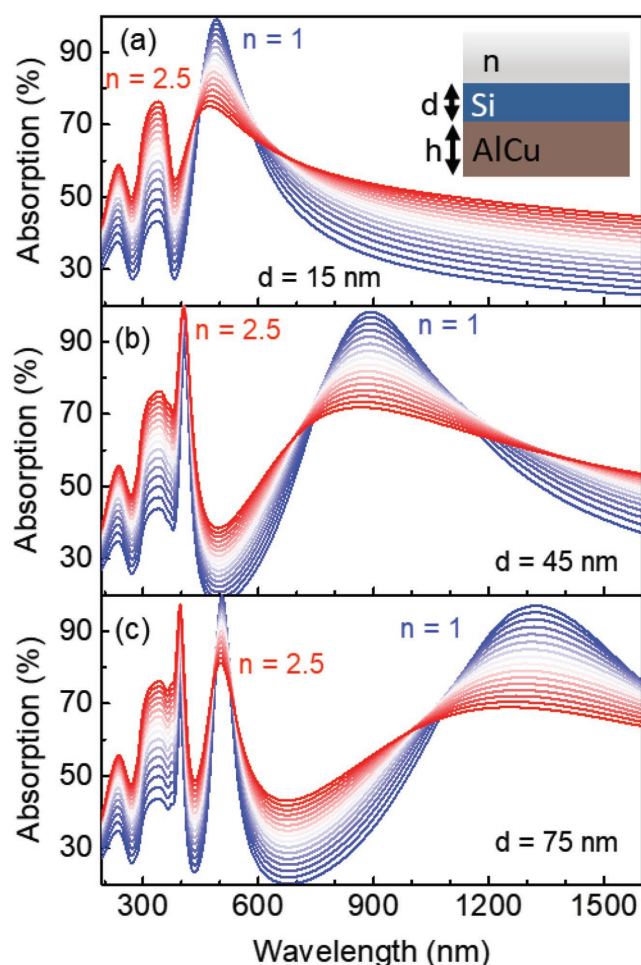


**Figure 4.** Effect of surrounding media on metal alloyed-based superabsorbers. Calculated normal incidence absorption spectra of Si/AlCu with a semiconductor layer of a)  $d = 15$  nm, b)  $d = 45$  nm, and c)  $d = 75$  nm. The index of refraction of the surrounding medium ( $n$ ) varies from 1 (blue) to 2.5 (red). The inset in (a) displays a schematic of the superabsorber; out of scale for clarity.

Motivated by the multi-wavelength near-unity absorption behavior of the Si/AlCu system, we discuss in **Figure 4** the effect of the surrounding media on the absorption characteristics of the superabsorber. For all semiconductor thicknesses considered, at normal unpolarized incident light, the absorption maximum of Si/AlCu blue shifts while increasing the index of refraction ( $n$ ), changing from  $m_1$  to  $m_2$  or  $m_3$ . **Figure 4a** shows the near-unity absorption peak gradual shift from the visible range of the electromagnetic spectrum to the UV, from  $\lambda = 490$  nm (99.04%) to 341 nm (76.36%), for  $n = 1.0$  to 2.5, respectively. Similarly, **Figure 4b** presents the absorption maximum changing from  $\lambda = 895$  (98.2%) to 406 nm (99.95%) as  $n$  goes from 1.0 to 2.0 when  $d = 45$  nm. Lastly, **Figure 4c** shows a transition from a dual- to a single-band superabsorber. For  $n = 1$ , there are two peaks with extremely high absorption, one at  $\lambda = 1319$  nm (96.97%) and another at  $\lambda = 506$  nm (99.93%). As  $n$  increases, the absorption peak at  $\lambda = 397$  nm also increases, reaching a maximum of 97.25% for  $n = 2.5$ .

As a proof of concept, we fabricate a-Si/AlCu thin film superabsorbers (see the Experimental Section for details of the fabrication and measurements, and **Figure S14** and **S15** in the Supporting Information for sample details). **Figure 5** shows the measured and calculated absorption maps as a function of  $\theta$  and  $\lambda$  for 95 nm AlCu metallic films coated with 6, 53, and 94 nm a-Si. The resonant peak redshifts as the thickness of the semiconductor increases. For all cases presented here, the multi-wavelength near-unity absorption of the a-Si/AlCu system is  $>85\%$  for a wide angle of incidence. In particular for  $d = 6$  nm the mode  $m_1$  at  $\lambda = 216$  nm spans over  $40^\circ$  (**Figure 5a**). Likewise, for  $d = 53$  nm at  $\lambda = 645$  nm the maximum absorption goes up to  $70^\circ$  (**Figure 5c**). For the sample with  $d = 94$  nm, we obtain a dual-band superabsorber, where an absorption  $>85\%$  is maintained up to  $70^\circ$  for the two modes ( $\lambda = 451$  and 1062 nm). Our experimental results are in good agreement with the calculations, as presented in **Figures 5b,d,f**, where peak position, intensity, and maximum angle of incidence match.

Here, we provide a guide for obtaining superabsorption through a lithography-free, CMOS-compatible approach that can be easily scaled up. We show numerical and experimental evidence that the alloying of Al and Cu metals yields a unique permittivity, not obtained by its pure counterparts. When combined with a thin film semiconductor layer this alloy enables near-unity and multi-wavelength absorption. According to the phase diagram of Al-Cu,<sup>[40]</sup> we speculate that our AlCu could be a disordered material, with lower electron mean free path when compared to both pure Al and Cu.<sup>[41]</sup> In turn, this leads to a higher value of the imaginary part of the permittivity in the NIR region for the alloy (see **Figure S2** in the Supporting Information). Thus, the combination of the strength of the polarization generated by an external electric field (small  $|\epsilon_1|$ ) and the losses in the metal (large  $\epsilon_2$ ) provides the ideal condition for tuning the wavelength of the near-unity absorption ( $>99\%$ ) ranging from the visible to the NIR.

In conclusion, we presented a multi-wavelength, polarization-independent and wide-angle near-unity superabsorber formed by a semiconductor/AlCu metal-alloyed thin film stack. For the metallic material, we designed an alloy of Al and Cu that outperforms pure metals. A complete description of the light absorption within the stack, using TMM and numerical simulations demonstrated that ultrahigh absorption ( $>99\%$ ) arose from the Si/AlCu system, where the peak could be finely tuned from visible to NIR by increasing the thickness of the semiconductor layer. Absorption maps of the incident angle for an unpolarized light confirmed its omnidirectionality, where 95% of light was absorbed within  $50^\circ$  from the normal incidence angle and decreasing slightly to 80% at  $70^\circ$ . The index of refraction of the surrounding media was found to be an efficient knob to promote the second and third optical modes with maximum absorption. Additionally, we obtained a dual-band superabsorber with a planar Si/AlCu structure, with both peaks presenting absorption  $>98\%$ . To validate our predictions, we fabricated a-Si/AlCu superabsorbers and confirmed that near-unity single- and dual-band responses are achieved by simply changing the thickness of the semiconductor layer. Superabsorbers containing an engineered AlCu metal alloy thin film could have a significant impact in applications such as sensors, photodetectors, optical

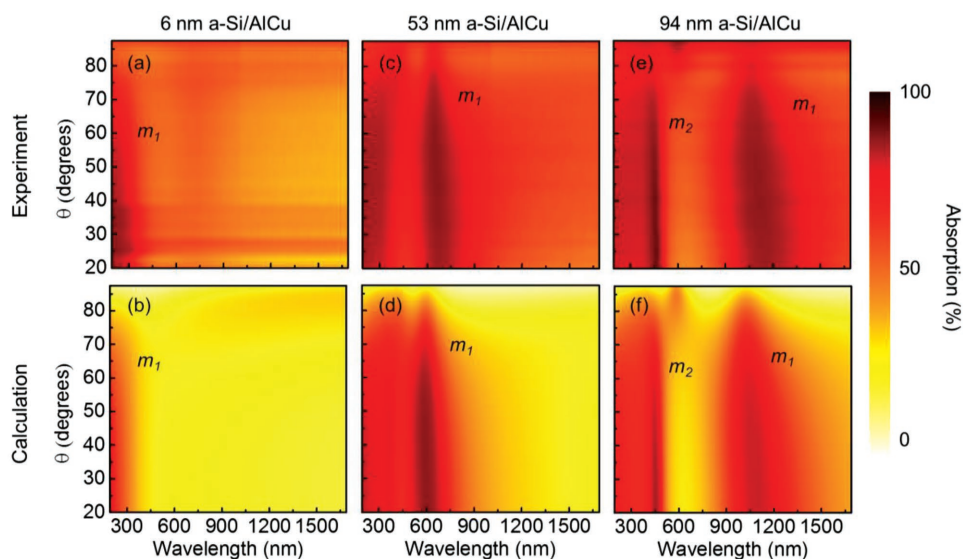


**Figure 5.** Experimental demonstration of a-Si/AlCu superabsorbers. Measured and calculated absorption maps as a function of incident angle  $\theta$  and wavelength for 95 nm AlCu metallic films coated with a,b) 6, c,d) 53, and e,f) 94 nm of Si.

filters, and radar technologies due to their high performance and straightforward scalability in size, overcoming the current challenges of incorporating nanostructures. Further, the potential compatibility with well-established CMOS fabrication processes could likely enable low-cost, mass production of nanophotonic devices incorporating these earth-abundant metal alloys. We foresee this new material as a promising alternative to modulate the optical response of active components in photonic devices. By varying the chemical composition of the alloyed metals, one can reach responses not obtained by pure elements.

## Experimental Section

**Sample Fabrication:** Ag, Au, Al, Cu, AlCu thin films were deposited by sputtering/cosputtering, and Cr was deposited through thermal evaporation on glass substrates, which were cleaned with deionized water, acetone, and dried with  $N_2$  before the deposition step. The deposition rate was  $5.5 \text{ nm min}^{-1}$  for Al, Cu, and AlCu,  $53 \text{ nm min}^{-1}$  for Ag,  $38 \text{ nm min}^{-1}$  for Au, and  $6 \text{ nm min}^{-1}$  for Cr. All deposition rates were calibrated by adjusting the power of each metal source based on the film thickness determined by ellipsometry. During the deposition, the glass substrate was rotated at 8 rpm to obtain a uniform chemical composition for the thin films. Note that the fabricated Cr sample is metallic in the visible despite the presence of Cr oxide that commonly results from thin film deposition.<sup>[42]</sup> For the superabsorber samples, a-Si was deposited on AlCu alloyed thin film and glass by e-beam evaporation at a rate of  $1.5 \text{ \AA s}^{-1}$ . The sample holder was rotated at a speed of 50 rpm during the deposition. The a-Si thickness and permittivity were determined using ellipsometry.

**Dielectric Function Model:** The ellipsometry measurements were performed using a J. A. Woollam spectroscopic ellipsometer (wavelength range: 193–1680 nm) to record both reflection and transmission spectra. The reflection measurements were acquired at  $60^\circ$ ,  $65^\circ$ , and  $70^\circ$  and the transmission was performed at  $0^\circ$  (from the normal incidence). A B-spline model was applied to extract the dielectric function for each metallic thin film, as reported previously.<sup>[29]</sup> For all metallic films, the mean square error of all fits was  $<6$ . Ellipsometry was used to determine the thickness of the sample less than 100 nm, otherwise the thicknesses were obtained by profilometer.

**Absorption Maps:** The absorption maps were obtained based on the reflection maps by considering zero transmission for Si/AlCu stack (Figure S11, Supporting Information), which were measured by ellipsometry. Baseline measurements were performed at each incident angle using a standard 25 nm  $\text{SiO}_2/\text{Si}$  wafer.

**Elemental Analysis:** The elemental analysis for the AlCu alloyed thin film was performed by energy-dispersive X-ray spectroscopy in a scanning electron microscope (SEM) system (see Table S1 in the Supporting Information). These measurements were acquired on three  $20 \times 20 \text{ }\mu\text{m}^2$  representative regions of the sample, and showed a chemical composition of  $\text{Al}_{0.55}\text{Cu}_{0.45}$ . To determine the atomic ratio between Al and Cu, the quantification was performed for each location after acquiring the signals for 2 min and 40 s.

**Transfer Matrix Method:** The TMM was used to calculate the transmission ( $T$ ) and reflection ( $R$ ) coefficients of an incident plane wave propagating along the  $z$ -axis through a thin layer of semiconductor on top of a metal substrate. Therefore, light absorption ( $A$ ) was computed as  $A = 1 - R - T$ . For an optically thick film  $T = 0$ ; and  $A = 1 - R$ . In this stack configuration, the field within one layer can be represented as the superposition of left- and right-traveling electromagnetic waves. Applying the proper boundary conditions, one can describe the propagation of the waves in the matrix form as

$$\begin{pmatrix} E_{i0} + E_{r0} \\ (E_{i0} - E_{r0})\gamma_0 \end{pmatrix} = M_1 \cdot M_2 \cdots M_N \begin{pmatrix} E_t \\ \gamma_t E_t \end{pmatrix} = M_{\text{tot}} \begin{pmatrix} E_N \\ \gamma_N E_N \end{pmatrix} \quad (1)$$

$$= \begin{pmatrix} m_{11} & m_{12} \\ m_{21} & m_{22} \end{pmatrix} \begin{pmatrix} E_N \\ \gamma_N E_N \end{pmatrix}$$

where  $E_{i0}$ ,  $E_{r0}$ , and  $E_t$  are the incident, reflected, and transmitted electric fields for a system containing  $N$  layers. For each layer  $j$  the transfer matrix is given by

$$M_j = \begin{pmatrix} \cos \delta_j & \frac{i \sin \delta_j}{\gamma_j} \\ i \gamma_j \sin \delta_j & \cos \delta_j \end{pmatrix} \quad (2)$$

with  $\delta_j = \omega \tilde{n}_j d_j \cos \theta_j / c$ ,  $\cos \theta_j = \tilde{n}_j^{-1} \sqrt{\tilde{n}_j^2 - \tilde{n}_0^2 \cos^2 \theta_0}$ , and  $\gamma_j = \tilde{n}_j \cos \theta_j$  for TE polarization and  $\gamma_j = \tilde{n}_j / \cos \theta_j$  for TM polarization. Thus, the reflection and transmitted amplitudes are written as

$$r = \frac{\gamma_0 m_{11} + \gamma_0 \gamma_t m_{12} - m_{21} - \gamma_t m_{22}}{\gamma_0 m_{11} + \gamma_0 \gamma_t m_{12} + m_{21} + \gamma_t m_{22}} \quad \text{and} \quad t = \frac{2\gamma_0}{\gamma_0 m_{11} + \gamma_0 \gamma_t m_{12} + m_{21} + \gamma_t m_{22}} \quad (3)$$

where  $R = |r|^2$ ,  $T = |t|^2 k_t/k_i$  ( $k_i$  and  $k_t$  are the transmitted and incident wave numbers).

**Numerical Simulations:** The finite-difference time-domain method was used to simulate the 3D full-field light-matter interactions, with a normally incident plane wave as the light source. A thin layer of semiconductor on top of a metal was used in the simulation space. Perfect matched layer boundary conditions were applied in the z-direction while periodic boundary conditions were used in the x- and y- in-plane directions. The broadband radiation of the plane wave light source was propagated from air into the stack with the semiconductor on the front, as shown in the schematic of Figure 1. For all simulations presented here, the index of refraction of Ag, Au, Cr, Al, Cu, AlCu, and a-Si was modeled through the multi-coefficient material model using transmission and reflection ellipsometry measurements of thin films as the input data (see Figures S1 and S2 in the Supporting Information). For Si, Ge, and GaAs, data from Palik<sup>[43]</sup> was used. The cross-section distribution profiles of the absorbance were calculated as a function of wavelength for each simulation.

## Supporting Information

Supporting Information is available from the Wiley Online Library or from the author.

## Acknowledgements

M.R.S.D. and C.G. contributed equally to this work. The authors thank L. J. Kraye, E. M. Tennyson, and N. Hong (from J.A. Woollam) for fruitful discussions, and the Maryland NanoCenter FabLab for their technical support. C.G. thanks the support from Y. G. Liang for the AFM measurement. The authors acknowledge the financial support from the National Science Foundation Grants No. 16-09414 (DMR) and HRD1008117 (ADVANCE program), from the Schlumberger Foundation Faculty for the Future, from the 2017 UMD Graduate Summer Fellowship, and from the 2017-2018 Harry K. Wells Graduate Fellowship.

## Conflict of Interest

The authors declare no conflict of interest.

## Keywords

alloyed thin films, aluminum, copper, permittivity, superabsorbers

Received: August 5, 2017

Revised: October 7, 2017

Published online: December 13, 2017

[1] R. Walter, A. Tittl, A. Berrier, F. Sterl, T. Weiss, H. Giessen, *Adv. Opt. Mater.* **2015**, *3*, 398.

[2] T. D. Dao, S. Ishii, T. Yokoyama, T. Sawada, R. P. Sugavaneshwar, K. Chen, Y. Wada, T. Nabatame, T. Nagao, *ACS Photonics* **2016**, *3*, 1271.

- [3] M. Farhat, T.-C. Cheng, K. Q. Le, M. M.-C. Cheng, H. Bağcı, P.-Y. Chen, *Sci. Rep.* **2016**, *6*, 19984.
- [4] Z. J. Coppens, I. I. Kravchenko, J. G. Valentine, *Adv. Opt. Mater.* **2016**, *4*, 671.
- [5] C. Yang, C. Ji, W. Shen, K.-T. Lee, Y. Zhang, X. Liu, L. J. Guo, *ACS Photonics* **2016**, *3*, 590.
- [6] N. Liu, M. Mesch, T. Weiss, M. Hentschel, H. Giessen, *Nano Lett.* **2010**, *10*, 2342.
- [7] J. Perini, L. S. Cohen, *IEEE Trans. Electromagn. Compat.* **1993**, *35*, 223.
- [8] Y. J. Yoo, S. Ju, S. Y. Park, Y. Ju Kim, J. Bong, T. Lim, K. W. Kim, J. Y. Rhee, Y. Lee, *Sci. Rep.* **2015**, *5*, 14018.
- [9] N. Landy, S. Sajuyigbe, J. Mock, D. Smith, W. Padilla, *Phys. Rev. Lett.* **2008**, *100*, 207402.
- [10] E. Knott, J. F. Shaeffer, M. T. Tuley, *Radar Cross Section*, Scitech, Raleigh **2004**.
- [11] G. T. Ruck, D. E. Barrick, W. D. Stuart, *Radar Cross Section Handbook*, Plenum, New York **1970**.
- [12] Y. Ra'di, C. R. Simovski, S. A. Tretyakov, *Phys. Rev. Appl.* **2015**, *3*, 037001.
- [13] A. Tittl, P. Mai, R. Taubert, D. Dregely, N. Liu, H. Giessen, *Nano Lett.* **2011**, *11*, 4366.
- [14] G. M. Akselrod, J. Huang, T. B. Hoang, P. T. Bowen, L. Su, D. R. Smith, M. H. Mikkelsen, *Adv. Mater.* **2015**, *27*, 8028.
- [15] Y. Chen, X. Li, X. Luo, S. A. Maier, M. Hong, *Photonics Res.* **2015**, *3*, 54.
- [16] D. Hasan, P. Pitchappa, J. Wang, T. Wang, B. Yang, C. P. Ho, C. Lee, *ACS Photonics* **2017**, *4*, 302.
- [17] X. Zhao, J. Zhang, K. Fan, G. Duan, G. D. Metcalfe, M. Wraback, X. Zhang, R. D. Averitt, *Photonics Res.* **2016**, *4*, A16.
- [18] J. Yang, C. Gong, L. Sun, P. Chen, L. Lin, W. Liu, *Sci. Rep.* **2016**, *6*, 38732.
- [19] J.-B. You, W.-J. Lee, D. Won, K. Yu, *Opt. Express* **2014**, *22*, 8339.
- [20] H. Song, L. Guo, Z. Liu, K. Liu, X. Zeng, D. Ji, N. Zhang, H. Hu, S. Jiang, Q. Gan, *Adv. Mater.* **2014**, *26*, 2737.
- [21] J. Park, J.-H. Kang, A. P. Vasudev, D. T. Schoen, H. Kim, E. Hasman, M. L. Brongersma, *ACS Photonics* **2014**, *1*, 812.
- [22] M. A. Kats, R. Blanchard, P. Genevet, F. Capasso, *Nat. Mater.* **2013**, *12*, 4.
- [23] H. Kocer, S. Butun, Z. Li, K. Aydin, *Sci. Rep.* **2015**, *5*, 8157.
- [24] M. Yan, *J. Opt.* **2013**, *15*, 025006.
- [25] S. Shu, Z. Li, Y. Y. Li, *Opt. Express* **2013**, *21*, 25307.
- [26] W. Streyer, S. Law, G. Rooney, T. Jacobs, D. Wasserman, *Opt. Express* **2013**, *21*, 9113.
- [27] S.-T. Yen, P.-K. Chung, *Opt. Lett.* **2015**, *40*, 3877.
- [28] J. W. Cleary, R. Soref, J. R. Hendrickson, *Opt. Express* **2013**, *21*, 19363.
- [29] C. Gong, M. S. Leite, *ACS Photonics* **2016**, *3*, 507.
- [30] Y. Hashimoto, G. Seniutinas, A. Balčytis, S. Juodkazis, Y. Nishijima, *Sci. Rep.* **2016**, *6*, 25010.
- [31] C. Gong, M. R. S. Dias, G. C. Wessler, J. A. Taillon, L. G. Salamanca-Riba, M. S. Leite, *Adv. Opt. Mater.* **2017**, *5*, 1600568.
- [32] F. A. A. Nugroho, B. Iandolo, J. B. Wagner, C. Langhammer, *ACS Nano* **2016**, *10*, 2871.
- [33] N. Kinsey, M. Ferrera, V. M. Shalaev, A. Boltasseva, *J. Opt. Soc. Am. B* **2015**, *32*, 121.
- [34] J. Valentine, J. Li, T. Zentgraf, G. Bartal, X. Zhang, *Nat. Mater.* **2009**, *8*, 568.
- [35] M. A. Kats, F. Capasso, *Laser Photonics Rev.* **2016**, *10*, 735.
- [36] V. Fournée, I. Mazin, D. A. Papaconstantopoulos, E. Belin-Ferré, *Philos. Mag. Part B* **1999**, *79*, 205.



- [37] Y. Jiang, S. Pillai, M. A. Green, *Sci. Rep.* **2016**, 6, 30605.
- [38] H. Reddy, U. Guler, K. Chaudhuri, A. Dutta, A. V. Kildishev, V. M. Shalaev, A. Boltasseva, *ACS Photonics* **2017**, 4, 1413.
- [39] Y. Peng, W. Jiang, A. Eric, G. Alexander, W. Zhiming, *J. Phys. D: Appl. Phys.* **2016**, 49, 365101.
- [40] T. B. Massalski, *Bull. Alloy Phase Diagrams* **1980**, 1, 27.
- [41] F. E. Luborsky, *Amorphous Metallic Alloys (Butterworths Monographs in Materials)*, Butterworth & Co Ltd., Oxford, UK **1983**.
- [42] S.-F. Wang, H.-C. Lin, H.-Y. Bor, Y.-L. Tsai, C.-N. Wei, *J. Alloys Compd.* **2011**, 509, 10110.
- [43] E. D. Palik, *Handbook of Optical Constants of Solids*, Academic Press, San Diego, CA **2012**.